Acquisition of FDS for Oil-Immersed Insulation at Transformer Hotspot Region Based on Multiconstraint NSGA Model

Xianhao Fan ⓘ, Jiefeng Liu ⓘ, *Member, IEEE*, Hui Hwang Goh ⓘ, *Senior Member, IEEE*, Yiyi Zhang ⓘ, *Member, IEEE*, Chaohai Zhang ⓘ, *Member, IEEE*, and Saifur Rahman ⓘ, *Life Fellow, IEEE*

Abstract—The evaluation of the state of transformer oil-immersed insulation based on the traditional methods becomes unreliable due to the nonuniform aging effect. To address this issue, a novel model for accessing the aging information of transformer oil-immersed insulation at the hotspot is proposed. In this article, frequency-domain spectroscopy (FDS) is selected as the carrier for characterizing the aging states of oil-immersed insulation. The multiobjective function for reversing the FDS of the hotspot is constructed based on the dielectric response equivalent circuit. Then, the nondominated sorting genetic algorithm with the multiconstraint scheme is proposed to solve the multiobjective function, by which the FDS data of the transformer hotspot region are acquired. The verification results indicate that the average standard deviation between the computed FDS of the hotspot region and the measured data is less than 0.26. The contribution of this article is in the exploration of the proposed model as a potential tool to extract the FDS data of the hotspot region. This will promote a more reliable aging evaluation of the transformer oil-immersed paper insulation at the hotspot.

Index Terms—Frequency-domain spectroscopy (FDS), hotspot temperature, multiobjective optimization, oil-immersed insulation, transformer.

Nomenclature

ω and ξ	Angular frequency and response constant.
X and Y	Geometrical parameters of the insulation system.
ε^*_r	Complex relative permittivity.
ε'_r and ε''_r	Real and imaginary parts of ε^*_r.
T_g	Temperature gradient.
m	Total number of aging states.
Θ	Combined coefficients.
fp and $\tan \delta$	Frequency point and dispersion loss factor.
φ and Ω	Objective function and variable set.
g_s	Linear inequality constraints.
Υ	Total number of linear inequality constraints.
α and λ	Coefficients used in g_s.
ϕ	Penalty function.
v_r and c	Comparison factor and comparison criterion.
lr	Rank of the solution.
D_{rank}	Total classes of population grading.
η and α	Penalty degree and constraint coefficient.
F	Individual fitness function.
$L_{r\min}$ and $L_{i\min}$	Lower limit of real and imaginary parts of ε^*_r.
$U_{r\min}$ and $U_{i\min}$	Upper limit of real and imaginary parts of ε^*_r.
lb_r and lb_i	Lower limit coefficient of real and imaginary parts.
ub_r and ub_i	Upper limit coefficient of real and imaginary parts.
Abbreviations	
FDS	Frequency-domain spectroscopy.
PDC	Polarization depolarization current.
DP and mc%	Degree of polymerization and moisture content.
NSGA	Nondominated sorting genetic algorithm.
PS and Gen	Population size and maximum generations.
CP	Crossover probability.
MI and MP	Migration Interval and mutation probability.

TN	Total number of Pareto optimal solution.
STD and RE	Standard deviation and relative error
Superscript and Subscript	
i	Serial number of aging states.
j	Serial number of independent variables.
l and k	label of individuals.
p and o	Oil-immersed pressboard and insulating oil.
tot	Insulation system.
c and m	Calculated value and measured value.

I. INTRODUCTION

AS OF 2021, China has operated ultrahigh-voltage (UHV) transmission lines with a cumulative line length of more than 41 000 km, with a cumulative power transformation capacity of about 2.1 trillion kWh. A large number of transformers [1], cables [2], bushings [3], insulators [4], and other critical power equipment operate on the power transmission line, which is responsible for power conversion, transmission, electrical connection, and mechanical support. Over time, the insulating materials in the aforementioned electrical equipment will deteriorate due to the effects of the electric field, thermal field, and mechanical stress, resulting in abrupt failure and jeopardizing the modern power grid's stability. Thus, condition assessment and operation monitoring of the power equipment and their insulation systems are critical for assuring the safety of UHV projects while also extending their service life [5], [6].

When transformers are energized, their internal temperature rises, and the inner geometrical structure and iron core (winding) radiate, creating a temperature gradient perpendicular (and parallel) to the iron core [8]. As a result of extended exposure to temperature gradients, the distribution of insulation aging degree is proportional to winding height and inversely proportional to winding distance [8], [9]. In this case, the insulation system suffers the nonuniform aging, also, the insulation at the hotspot sustains the worst deterioration and finally debases the operation safety and remaining life of power equipment [8]. Thus, in comparison to other positions, the condition of oil-immersed insulation at the hotspot is more critical. Reviewing the existing methods, several branches of the technique involving the electrical, chemical, and physical methodology are reported to implement the state evaluation, including partial discharge [10], dissolved gases analysis [11], dissolved chemical indicator (furfural, methanol, etc.) [8], and dielectric response technique [7]. Specifically, the dielectric response technique has been used to evaluate the aging state of oil-immersed insulation due to its nondestructive property and sensitivity to degradation. However, the existing methods are developed based on the assumption of uniform aging conditions. In this case, the evaluation results acquired are an approximate average value used to characterize the aging states of the entire insulation system rather than the "weakest point." Thus, the traditional methods would be debatable under nonuniform aging conditions.

In present research articles, the dielectric response technique has been employed for studying the potential connection between the presence of hotspots (or nonuniform aging) and the variation law of dielectric response data. In the literature [12], the experimental results show that the shape of dielectric response curves will alter regularly with the altering nonuniform aging states. Nevertheless, the curve analysis cannot deduce a quantitative result to describe either the variation law or property of the dielectric response. According to Debye relaxation theory [13], the electrical units combined in the form of equivalent circuits are capable of characterizing the various relaxation processes of the heterogeneous dielectric under an excitation voltage. Then, Baral and Chakravorti [7], [14] used the modified Maxwell model to simulate the polarization and conductivity behavior of oil-paper insulation under nonuniform aging, in which the correlation between branch parameters and presence of hotspots is proved. Cui *et al.* [15] proposed the concept of "time windows" to construct a distributed parameter model, and it also proved that the nonuniform aging effect will alter the model parameters. While such a connection is preliminarily used for characterizing the insulation state during nonuniform aging, it has not been established that it is only affected by the insulation state at the hotspot. As a result, the parameters or aging information retrieved from the frequency-domain spectroscopy (FDS) of the hotspot's insulation are more dependable for describing its aging states.

The *XY* model is introduced to bridge the FDS between the entire system and its components (including oil gap, barrier, and spacer) [16]. Consequently, provided that the FDS data of insulation at the hotspot can be extracted by using an equivalent circuit model, the aging condition evaluation of the hotspot can be readily completed by using the existing FDS based methods. By virtue of this, we proposed the modified *X* model to study the relationship of FDS data between the bushing insulation system and its solid insulation under nonuniform aging [17]. Furthermore, a modified *XY* model [18], which aims to build the connection between the transformer insulation system and its components under nonuniform aging, is also proposed. However, in these models, the FDS data for the hotspot are presumed to be known before utilizing it to predict the FDS data for the entire system. In other words, the equivalent "inverse process," i.e., obtaining the FDS data for the transformer hotspot zone from the overall measurement FDS data, is not complete. Thus, if the "inverse process" can be addressed, the standard FDS approach (established under the uniform aging conditions) for aging state analysis of hotspots will be inspired.

Given this issue, evolutionary algorithms are applied to address a variety of inverse problems involving optimization designs or solutions. In [19], the optimal multivariate variables of the dielectric response equivalent model are determined by using the Cuckoo search optimization algorithm, and then a simulation model is constructed to improve the time consumption of the FDS measurement. To minimize the total power loss of a three-phase transformer, the literature [20] proposes a globally feasible

method based on the use of NSGA-II+FEM to achieve the optimal design of transformer characteristics. This heuristic search algorithm can also be used to estimate the high-frequency model parameters of power transformers [21] and for the noniterative design of the high-frequency transformers [22].

In that respect, this article proposed a dielectric response equivalent circuit-based multiobjective optimization model for obtaining FDS data from oil-immersed insulation at the hotspot. In this article, the composite structure and its equivalent circuit are constructed to simulate the nonuniform aging impact on its FDS data. Then, the multiobjective functions are defined and used to inverse the FDS data of each component contained in the entire system. The nondominated sorting genetic algorithm with the multiconstraint scheme (MC-NSGA) is later proposed to solve the objective functions, by which the FDS data of the hotspot can be acquired. Finally, the verification and comparing results are presented to examine the suggested model's viability and accuracy. The contribution of this article is to extract the FDS of the hotspot from the total data of the entire insulation system hence facilitating the investigation of the hotspot's insulation state.

II. EQUIVALENT CIRCUIT MODEL FOR QUANTIFYING FDS DATA UNDER NONUNIFORM AGING

To quantitatively analyze or connect the FDS between the transformer insulation system and the contained components (spacer, barrier, and oil) under uniform aging, the *XY* model is proposed, as is shown in the following equation [16]:

$$\varepsilon^*_{\text{rtot}}(\omega) = \frac{1 - Y}{\frac{1-X}{\varepsilon^*_{\text{ro}}(\omega)} + \frac{X}{\varepsilon^*_{\text{rp}}(\omega)}} + \varepsilon^*_{\text{rp}}(\omega) \cdot Y \qquad (1)$$

where ω is the angular frequency, $\varepsilon^*_{\text{rp}}$, $\varepsilon^*_{\text{ro}}$, and $\varepsilon^*_{\text{rtot}}$ are the complex relative permittivity of the solid insulation, oil gap, and insulation system, respectively. *X* and *Y* are the geometric parameters of the insulation system, which are shown in the following equation [16]:

$$\begin{cases} X = \frac{\text{Thickness of barrier}}{\text{Thickness of main insulation}} \\ Y = \frac{\text{Width of spacer}}{\text{Average width of main insulation}} \end{cases} . \qquad (2)$$

However, the iron core (or winding) temperature of the energized transformer is generally much higher than its normal oil temperature. Thus, the temperature of oil-immersed paper insulation on different locations in the transformer main insulation system changes with the altering distance from the iron core [7], [14]. In this case, a temperature gradient (T_g) would be formed and then leads to the nonuniform aging of the oil-immersed insulation along the radial direction. Such a phenomenon can be illustrated by using Fig. 1.

In this case, the traditional *XY* model is incapable of connecting the FDS data from the entire insulation system and its components. Thus, a modified equivalent circuit (modified *XY* model) was developed in [18] for establishing FDS connections between the entire system and its various components when nonuniform aging is considered, as illustrated in Fig. 2.
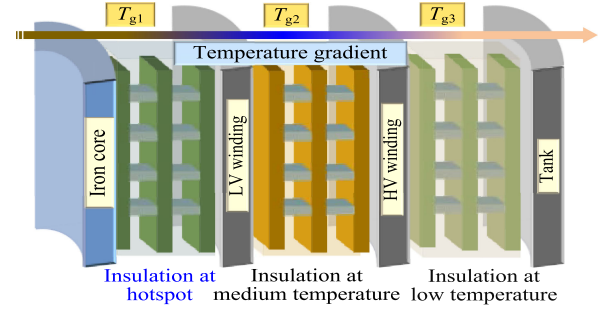

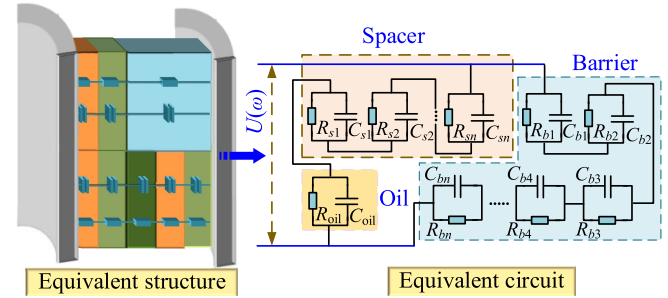Fig. 1. Nonuniform aging of transformer oil-immersed insulation.

Fig. 2. Equivalent circuit (modified *XY* model) of the insulation system.

Resistance (*R*) and capacitance (*C*) are used to describe the contribution of conductance and polarization behavior, respectively. The combination of these elements is used to illustrate the dielectric response property of oil-immersed insulation with various aging degrees. Then, the mathematical expression for bridging the complex relative permittivity of the liquid insulation (oil), solid insulation (barrier and spacer), and entire insulation system is expressed by the following equation according to Fig. 2 [18]:

$$\varepsilon^*_{\text{rtot}}(\omega)$$
$$= \xi^*(\omega) \cdot \left[\frac{mY}{\sum_{i=1}^{m} \frac{1}{\varepsilon^*_{\text{rp}\,i}(\omega)}} + \frac{1 - Y}{\frac{1-X}{\varepsilon_{\text{ro}}(\omega)} + \frac{X}{m}\left(\sum_{i=1}^{m} \frac{1}{\varepsilon^*_{\text{rp}\,i}(\omega)}\right)} \right] \qquad (3)$$

where ξ is a response constant, *i* is the categories of aging degree contained in the main insulation system, and *m* is the total number of aging states.

III. CONSTRUCTION OF COMPOSITE INSULATION STRUCTURE FOR SIMULATING NONUNIFORM AGING

A. Preparation of the Oil-Immersed Paper Insulation

The aging degrees of oil-immersed (paper) insulation in the entire system in Fig. 1 could be divided into three categories in the radial direction (T_{g1} to T_{g3}). To further analyze this phenomenon, a composite structure is constructed utilizing numerous pressboards (type I and type II) with varying degrees of polymerization (DP), as illustrated in Fig. 3.

The insulating oil is the Karamay No. 25 naphthenic mineral oil, the pressboard types I and II are utilized, and the insulating
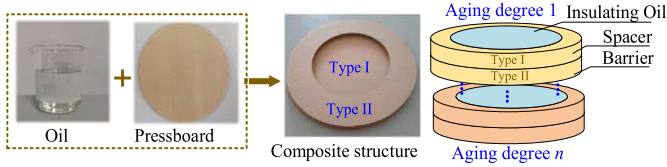
Fig. 3. Composite structure for simulating the radial nonuniform aging of transformer oil-immersed paper insulation.

TABLE I
DETAILS OF USED CELLULOSE PRESSBOARDS AND OIL

Pressboard I (Type I)		Pressboard II (Type II)	
Thickness	0.5 mm	Thickness	1 mm
Diameter	160 mm	Internal diameter	98 mm
Tensile strength	MD: 98 MPa, CMD: 47 MPa	Tensile strength	MD: 105 MPa, CMD: 80 MPa
Density	0.96 g/cm^3	Density	1.09 g/cm^3
Insulating oil			
Density (20℃)	Pour point	Flashpoint	Breakdown voltage
885.3 Kg/m^3	-49 ℃	138 ℃	65 kV

TABLE II
ARRANGEMENT OF COMPOSITE STRUCTURE WITH PRESSBOARDS

Structure	PB1	PB2	PB3	PB4
Structure 1	Elect	Elect	\	Elect
Structure 2	Elect	\	Elect	Elect
Structure 3	\	Elect	Elect	Elect

oil, which are specified in Table I. The pretreatment experiment is performed at 105 °C/50 Pa to prepare the dried pressboard and degassed oil. The accelerated thermal aging is then performed at 150 °C/50 Pa to prepare the oil-immersed pressboards with different DP and similar moisture. The preceding steps are consistent with established methods and guidelines in [17] and [18]. To ensure that the final results are not influenced by experimental error, the initial DP of pressboards after pretreatment should be about 1000, the inside moisture content should be less than 1%, and the initial moisture of oil should be less than 20 ppm (mg/kg).

According to Fig. 3, the prepared pressboards 1–4 (i.e., PB1 to PB4) with four aging states (corresponding to DP = 1054, 647, 520, and 275) and similar moisture content (0.91%, 0.81%, 0.79%, and 0.90%) are used to construct the composite structure to service the further analysis, and the contained worst aging state is coincident, which is listed in Table II. To minimize the impact of irrelevant factors on the analysis results, the values of X and Y in (3) of all prepared structures are set to 0.33 and 0.25, respectively. The temperature of the test chamber is maintained at 45 °C.

B. FDS Measurement of Composite Insulation Structure

The constructed composite structures presented in Table II are selected for performing the FDS test with the help of the measurement platform shown in Fig. 4, including the DI-RANA/OMICRON (dielectric loss range: 0–100; capacitance range: 10 pF to 100 μF) and a three-electrode test cell. The measurement range is 2×10^{-4}–5×10^3 Hz, measurement
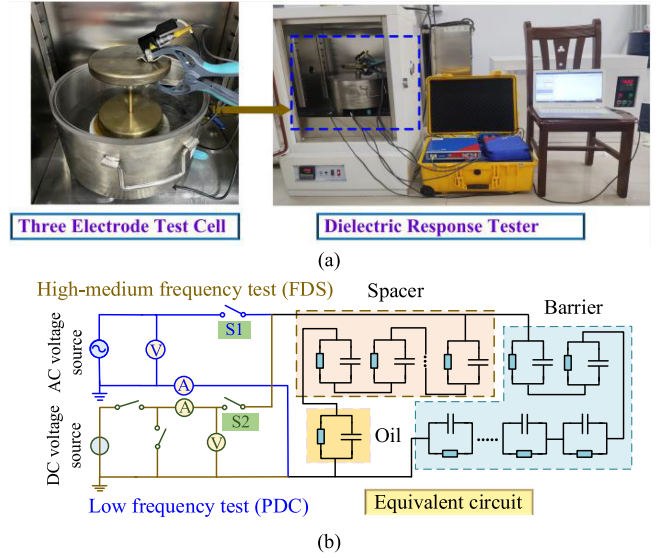

Fig. 4. FDS measurement platform. (a) Profile display. (b) Equivalent circuit of FDS measurement.

voltage/current is ac 200 V_{peak}/± 50 mA$_{\text{peak}}$, measurement form is FDS (test in high-medium frequency regions) + PDC (test in low-frequency regions), the required time is about 40 min, and test temperature maintains at 45 °C.

Relying on Fig. 4, the complex relative permittivity $\varepsilon^*(\omega)$ of single oil-immersed pressboards (PB1 to PB4), the composite structure (shown in Table II), and oil are measured and plotted in Fig. 5. The pressboard (PB4) conveys the worst aging state (i.e., lowest DP) in contrast to other pressboards contained in the same composite structure, thus, the measured FDS of PB4 is used to characterize the aging information of oil-immersed paper insulation at the hotspot.

IV. MC-NSGA-BASED MULTIOBJECTIVE OPTIMIZATION MODEL FOR ACCESSING FDS DATA OF HOTSPOT

From Fig. 5, the FDS data of single pressboard and composite structure are quite diverse, in this case, we cannot implement the aging evaluation of transformer oil-immersed insulation at the hotspot by directly using the FDS of the entire system. From (3), the modified *XY* model built the connection between the FDS data of the entire insulation system and their independent components (mainly including the oil-immersed insulation with the different aging states), where $\varepsilon^*_{\text{ro}}$ and $\varepsilon^*_{\text{rtot}}$ can be directly measured and $\varepsilon^*_{\text{rp}i}$ is the unknown variable. If we can determine the unknown $\varepsilon^*_{\text{rp}i}$ by using known $\varepsilon^*_{\text{ro}}$ and $\varepsilon^*_{\text{rtot}}$, the FDS data of hotspot (i.e., $\varepsilon^*_{\text{rp3}}$) of solid insulation can be thus calculated. As for such a purpose, we initialize all of the variables ($\varepsilon^*_{\text{rp}i}$), then $\varepsilon^*_{\text{rtot}}$ can be calculated by using (3). Once the calculated value is similar to the measured value of $\varepsilon^*_{\text{rtot}}$, the initial value of $\varepsilon^*_{\text{rp}i}$ is exactly the solution of the equation. Thus, three crucial steps are introduced herein to solve the mentioned issue.

1) Section IV-A aims to quantify the fitness of the solutions by using the defined multiobjective function group.
2) Section IV-B aims to find all solutions of the multiobjective function group by using the NSGA.
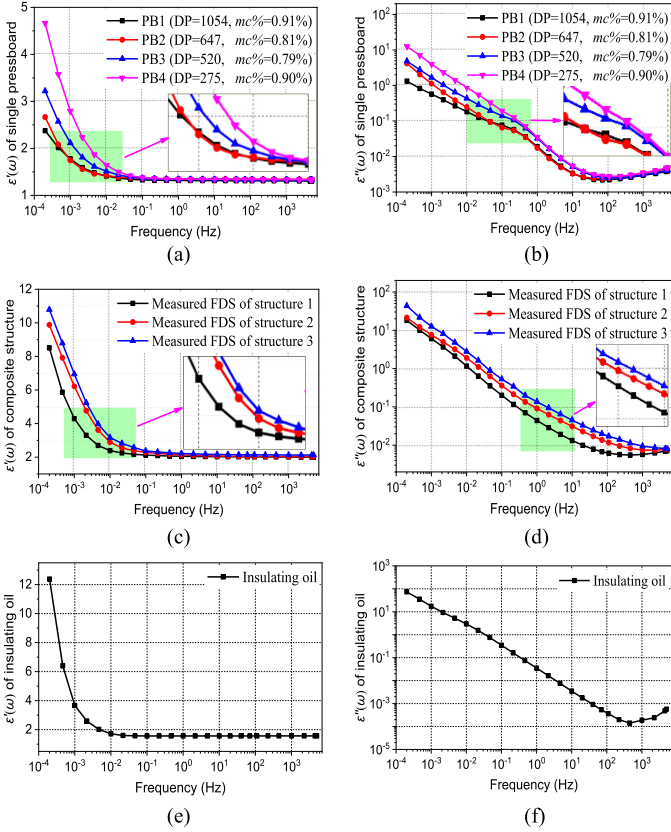
Fig. 5. Measured complex relative permittivity. (a) and (b) Real and imaginary parts of single pressboard PB1 to PB4. (c) and (d) Real and imaginary parts of composite structures 1–3. (e) and (f) Real and imaginary parts of insulating oil.

3) Section IV-C aims to determine a unique solution by using the defined multiconstraint scheme of NSGA (MC-NSGA).

The logic scheme of the defined procedure for achieving the above goal is plotted in Fig. 6.

A. Construction of Multiobjective Function Group

1) Decoupling of Mathematical Expression of Equivalent Circuit: Combined with (3), the mathematical expression of the complex relative permittivity of composite structures 1–3 ($\varepsilon^*_{\text{rtot}}$) can be illustrated by the following equations when three aging degrees are included in the modified *XY* model:

$$
\varepsilon^*_{\text{rtot}} = \xi^* \cdot \left[\frac{mY}{\frac{1}{\varepsilon^*_{rp1}} + \frac{1}{\varepsilon^*_{rp2}} + \frac{1}{\varepsilon^*_{rp3}}} \right.
$$
$$
\left. + \frac{1 - Y}{\frac{1-X}{\varepsilon_{\text{ro}}} + \frac{X}{m}\left(\frac{1}{\varepsilon^*_{rp1}} + \frac{1}{\varepsilon^*_{rp2}} + \frac{1}{\varepsilon^*_{rp3}}\right)} \right] \tag{4}
$$

$$
\text{s.t.} \begin{cases} \varepsilon^*_{\text{rtot}}(\omega) = \varepsilon'_{\text{rtot}}(\omega) - j\varepsilon''_{\text{rtot}}(\omega) \\ \varepsilon^*_{\text{ro}}(\omega) = \varepsilon'_{\text{ro}}(\omega) - j\varepsilon''_{\text{ro}}(\omega) \\ \xi^*(\omega) = \xi'(\omega) - j\xi''(\omega) \end{cases}
$$

$$
\begin{cases} \varepsilon^*_{rp1}(\omega) = \varepsilon'_{rp1}(\omega) - j\varepsilon''_{rp1}(\omega) \\ \varepsilon^*_{rp2}(\omega) = \varepsilon'_{rp2}(\omega) - j\varepsilon''_{rp2}(\omega) \\ \varepsilon^*_{rp3}(\omega) = \varepsilon'_{rp3}(\omega) - j\varepsilon''_{rp3}(\omega) \end{cases} \tag{5}
$$

where $\varepsilon^*_{\text{rp}i}$ ($i = 1$ to 3) is the complex relative permittivity of pressboards referring to the descending order of their DP, and $\varepsilon^*_{\text{rp}3}$ is the FDS data of solid insulation at the hotspot.

Then, the decoupling of $\varepsilon^*_{\text{rtot}}$ is performed to separate its real part (ε'_{r}) and imaginary part (ε''_{r}) as

$$
\varepsilon'_{\text{rtot}}(\omega) = \xi'(\omega) \cdot \left[\frac{mY \cdot \Theta_1(\omega)}{\Theta_1{}^2(\omega) - \Theta_2{}^2(\omega)} + \frac{(1-Y) \cdot \Theta_3(\omega)}{\Theta_3{}^2(\omega) - \Theta_4{}^2(\omega)} \right] \tag{6}
$$

$$
\varepsilon''_{\text{rtot}}(\omega) = \xi''(\omega) \cdot \left[\frac{mY \cdot \Theta_2(\omega)}{\Theta_1{}^2(\omega) - \Theta_2{}^2(\omega)} + \frac{(1-Y) \cdot \Theta_4(\omega)}{\Theta_3{}^2(\omega) - \Theta_4{}^2(\omega)} \right] \tag{7}
$$

where Θ_1 to Θ_4 are the combined coefficients for simplifying the equations, and their formulas are as follows:

$$
\Theta_1(\omega) = \sum_{i=1}^{3} \frac{\varepsilon'_{rpi}(\omega)}{\varepsilon'_{rpi}(\omega)^2 - \varepsilon''_{rpi}(\omega)^2} \tag{8}
$$

$$
\Theta_2(\omega) = \sum_{i=1}^{3} \frac{\varepsilon''_{rpi}(\omega)}{\varepsilon'_{rpi}(\omega)^2 - \varepsilon''_{rpi}(\omega)^2} \tag{9}
$$

$$
\Theta_3(\omega) = \frac{(1-X) \cdot \varepsilon'_{\text{ro}}(\omega)}{\varepsilon'_{\text{ro}}(\omega)^2 - \varepsilon''_{\text{ro}}(\omega)^2} + \frac{X}{m} \cdot \Theta_1(\omega) \tag{10}
$$

$$
\Theta_4(\omega) = \frac{(1-X) \cdot \varepsilon''_{\text{ro}}(\omega)}{\varepsilon'_{\text{ro}}(\omega)^2 - \varepsilon''_{\text{ro}}(\omega)^2} + \frac{X}{m} \cdot \Theta_2(\omega). \tag{11}
$$

2) Definition of Multiobjective Function: If $\varepsilon^*_{\text{rp}i}$ in (4) is initialized within an available region, any point within this range could be used to compute the total FDS, i.e., $\varepsilon^*_{\text{rtotc}}$. Meanwhile, the total FDS of the entire insulation system can be measured using the measurement platform in Fig. 4, and labeled as $\varepsilon^*_{\text{rtotm}}$. Hence, if $\varepsilon^*_{\text{rtotc}}$ is equal to $\varepsilon^*_{\text{rtotm}}$, the initial value of $\varepsilon^*_{\text{rp}i}$ is exactly what we wanted since one cannot access them without destroying the insulation system to perform the sampling test in a real transformer. Meanwhile, the disagreement between $\varepsilon^*_{\text{rtotc}}$ and $\varepsilon^*_{\text{rtotm}}$ could be always observed, in this case, the variables ($\varepsilon^*_{\text{rp}i}$) are the potential solution of the following equations once their sum of square error reaches the minimum:

$$
\begin{aligned} \varphi_1(x_j{}^{(fp)}) &= [\varepsilon'_{\text{rtotm}}(\omega) - \varepsilon'_{\text{rtotc}}(\omega)]^2 \\ \text{s.t.} \varepsilon'_{\text{rtotc}}(\omega) &= \xi'(\omega) \cdot \left[\frac{mY \cdot \Theta_1(\omega)}{\Theta_1{}^2(\omega) - \Theta_2{}^2(\omega)} + \frac{(1-Y) \cdot \Theta_3(\omega)}{\Theta_3{}^2(\omega) - \Theta_4{}^2(\omega)} \right] \end{aligned} \tag{12}
$$

$$
\begin{aligned} \varphi_2(x_j{}^{(fp)}) &= [\varepsilon''_{\text{rtotm}}(\omega) - \varepsilon''_{\text{rtotc}}(\omega)]^2 \\ \text{s.t.} \varepsilon''_{\text{rtotc}}(\omega) &= \xi''(\omega) \cdot \left[\frac{mY \cdot \Theta_2(\omega)}{\Theta_1{}^2(\omega) - \Theta_2{}^2(\omega)} + \frac{(1-Y) \cdot \Theta_4(\omega)}{\Theta_3{}^2(\omega) - \Theta_4{}^2(\omega)} \right]. \end{aligned} \tag{13}
$$

Thus, (12) and (13) can be serviced as the objective functions (φ_1, φ_2). fp is the label of the sampling frequency points. The variable set $\Omega(x_j)$ is defined to minimize the objective functions
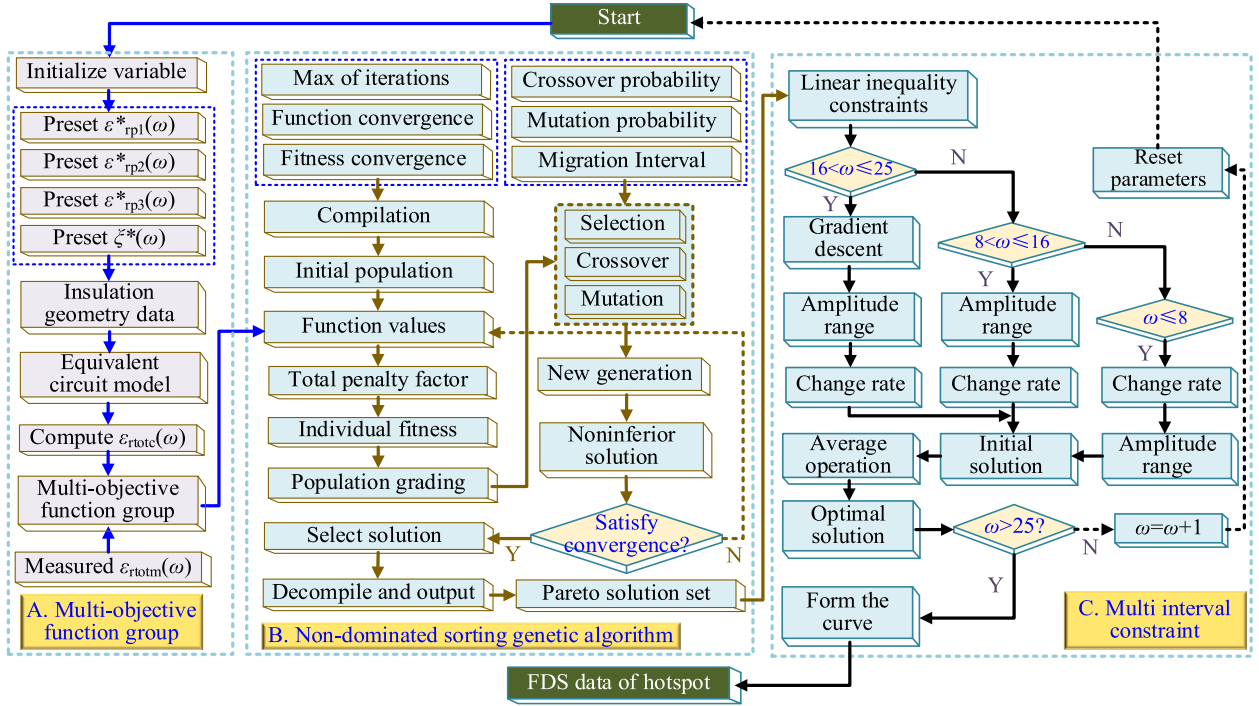
Fig. 6.   MC-NSGA-based multiobjective optimization model for accessing FDS data of oil-immersed insulation at hotspot.

(12) and (13)

$$\Omega(x_j) = \{\varepsilon'_{rp1}, \varepsilon'_{rp2}, \varepsilon'_{rp3}, \varepsilon''_{rp1}, \varepsilon''_{rp2}, \varepsilon''_{rp3}, \xi', \xi''\}$$
$$\text{s.t. lower bound} \leq x_j^{(fp)} \leq \text{upper bound}, j = 1, 2, \ldots, 8. \tag{14}$$

According to Debye relaxation, the dispersion loss factor ($\tan\delta$) is the ratio of the imaginary part to the real part, thus

$$\tan\delta_{\text{totm}}(\omega) = \varepsilon''_{\text{rtotm}}(\omega)/\varepsilon'_{\text{rtotm}}(\omega) \tag{15}$$

$$\tan\delta_{\text{totc}}(\omega) = \varepsilon''_{\text{rtotc}}(\omega)/\varepsilon'_{\text{rtotc}}(\omega). \tag{16}$$

Rely on the simultaneous analysis of both (12)–(16), another objective function (φ_3) is introduced in the view of the ratio between the real and imaginary parts

$$\varphi_3(x_j^{(fp)}) = [\tan\delta_{\text{totm}}(\omega) - \tan\delta_{\text{totc}}(\omega)]^2. \tag{17}$$

B. Solution-Based on NSGA Model

Each objective function can deduce an optimal solution. If only the single-objective function is solved, the results cannot guarantee the global optimal. The NSGA is thus used herein to get a solution set that satisfies multiobjective functions (12), (13), and (17). If the variable set $\Omega(x_j)$ can minimize the value of the objective function set $\varphi_r(x_j)$, the optimal solutions can be obtained, which satisfies the following equations:

$$\min \varphi_r(x_j^{(fp)}), r \in [1,3], j \in [1,8]$$
$$\text{s.t.} g_s(x_j^{(fp)}) < 0, s = 1, 2, \ldots, \Upsilon \tag{18}$$

$$g_s(x_j^{(fp)}) \propto \begin{bmatrix} \alpha_{11} & \alpha_{12} & \cdots & \alpha_{18} \\ \alpha_{21} & \alpha_{22} & \cdots & \alpha_{28} \\ \vdots & \vdots & \cdots & \vdots \\ \alpha_{\Upsilon 1} & \alpha_{\Upsilon 2} & \cdots & \alpha_{\Upsilon 8} \end{bmatrix} \cdot \begin{bmatrix} x_1^{(fp)} \\ x_2^{(fp)} \\ \vdots \\ x_8^{(fp)} \end{bmatrix}$$

$$- \begin{bmatrix} \lambda_1^{(fp)} \\ \lambda_2^{(fp)} \\ \vdots \\ \lambda_\Upsilon^{(fp)} \end{bmatrix} < 0 \tag{19}$$

where g_s is the linear inequality constraints of jth variables $x_j^{(fp)}$ during the initialization. Υ is the total number of linear inequality constraints, α is the coefficients used in constraint equations, and λ is the constants to hold the formula.

Then, the population grading is performed to determine which individual can enter the next round of evolution. The lower the grade of an individual, the more priority it is to be selected for the next round of evolution, and steps are as follows.

Step 1:

Employing factor v_r^{lk} to represent the comparison results of rth objective function values between individuals l and k. If the objective function of individual l (φ_l) is less than that of individuals k (φ_k), v_r^{lk} is equal to 1, thus

$$\begin{cases} \text{if } \varphi_l(x_j^{(fp)}) < \varphi_k(x_j^{(fp)}), v_r^{lk} = 1 \\ \text{if } \varphi_l(x_j^{(fp)}) = \varphi_k(x_j^{(fp)}), v_r^{lk} = 0 \\ \text{if } \varphi_l(x_j^{(fp)}) > \varphi_k(x_j^{(fp)}), v_r^{lk} = -1 \end{cases}. \tag{20}$$
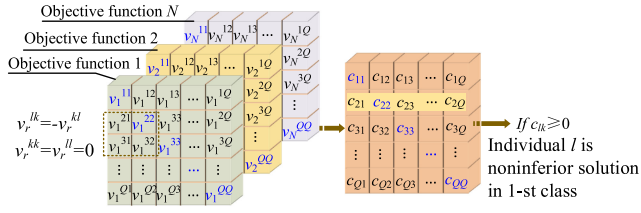
Fig. 7. Selection of the first-class noninferior solution in a population.

Fig. 8. Pareto front generated by multiobjective functions.

Step 2:

Criterion c_{lk} is used to describe the comparison result of objective functions between individual l and k. If individual l is better than individual k, then c_{lk} is equal to 1

$$\begin{cases} \text{if } (v_r^{lk} \geq 0 \,\&\,\& \sum_{r=1}^{N} v_r^{lk} > 0), c_{lk} = 1 \\ \text{if } (v_r^{lk} \leq 0 \,\&\,\& \sum_{r=1}^{N} v_r^{lk} < 0), c_{lk} = -1 \\ \text{else}, c_{lk} = 0 \end{cases} \quad (21)$$

Step 3:

The computed c_{lk} could form a matrix of order Q (population size), as shown in Fig. 7. If all c_{lk} in the lth line is equal or greater than 0, it indicates that l is similar or greater than the remaining individuals, in this case, l will be regarded as the first-class noninferior solution.

Step 4:

Deleting the lth row and column to perform the grading of the remaining individuals in this population.

Step 5:

Checking the individuals in other classes to generate the noninferior solution by comparing the function values.

Step 6:

Iteration operation could form a set of noninferior solutions generated by all populations.

The noninferior solution set is used to generate the offspring individuals by evolutionary operation (select, crossover, and mutation), and the final results would be obtained by referring to the following steps.

Step 1:

First, the penalty function (ϕ) in the following equations is used to reflect the impact of an individual's grade in its fitness calculation:

$$\phi(x_j^{(fp)}) = \phi_1(x_j^{(fp)}) + \phi_2(x_j^{(fp)}) \quad (22)$$

$$s.t. \, \phi_1(x_j^{(fp)}) = \sum_{m=1}^{O} \alpha_{pf} \cdot \left| min\{0, g_m(x_j^{(fp)})\} \right|^{\eta} \quad (23)$$

$$s.t. \, \phi_2(x_j^{(fp)}) = (lr - 1)/D_{rank} \quad (24)$$

where lr is the rank of the solution $x_j^{(fp)}$, D_{rank} is the total classes in the population grading, η is used to restrain the penalty degree and equal to 2, and α_{pf} is the penalty factor.

Step 2:

Then, the following equation is used to compute the individual fitness $F(x_j^{(fp)})$ of solution $x_j^{(fp)}$:
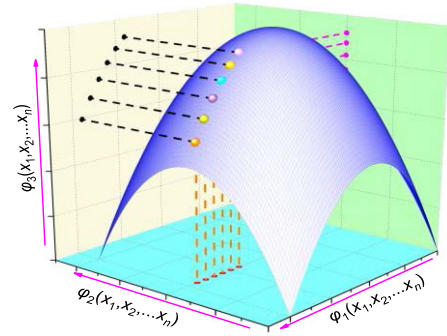
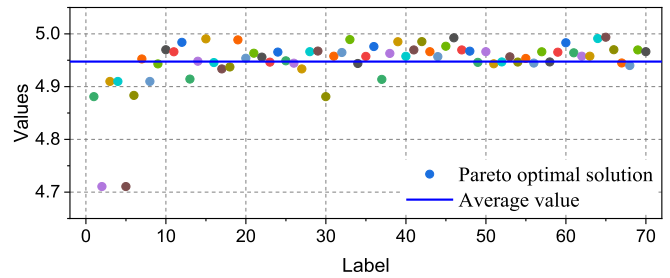$$F(x_j^{(fp)}) = 1/[1 + \phi(x_j^{(fp)})]. \quad (25)$$

Fig. 9. Distribution diagram of generated Pareto optimal solution.

Step 3:

The convergence judgment of $F(x_j^{(fp)})$ in Fig. 6 would determine whether the present solution $x_j^{(fp)}$ could be outputted as an optimal solution.

Step 4:

The algorithm model will find all solutions (i.e., variable set Ω) to form the Pareto front, such as Fig. 8.

From Fig. 8, any obtained Pareto solution is one in which an improvement in their fitness requires degradation of another. Thus, further constraint needs to be built to determine the unique solution.

C. Accessing the FDS Data of Hotspot Region by Using Multiconstraint Scheme of NSGA Model (MC-NSGA)

Out of Fig. 5, 25 frequency points have been measured during one FDS test. Each frequency point could trigger an entire optimization process to find all solutions. According to the data record, the total number of solutions of one variable contained in the same Pareto front could exceed 70. Fig. 9 is plotted by using all the Pareto optimal solutions of $x_j^{(fp)}$ ($fp = 1$, $j = 3$) to illustrate such a distribution. Most of the generated solutions fluctuate in a certain range, except for a few points with large deviations. In this case, determining how to acquire the unique solution that satisfies all constraints and requirements is critical for accessing the hotspot's FDS data via Pareto optimum solutions. This results in the introduction of a constraint scheme in multifrequency intervals to confirm the unique solution. The following processes are defined as following.
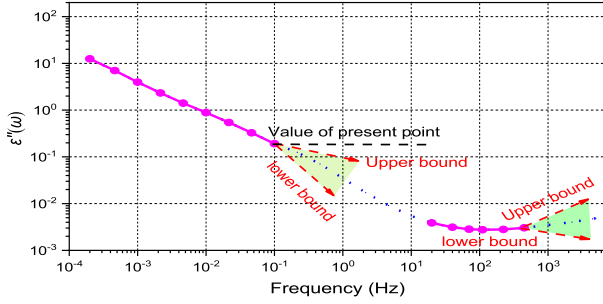
Fig. 10. Definition and determination of the amplitude coefficients.

Step 1:

All the frequency points are respectively divided into three intervals, including low frequency ($fp \leq 8$), medium frequency ($8 < fp \leq 16$), and high frequency ($16 < fp \leq 25$).

Step 2:

The intervals $[L_{r\min}\ U_{r\max}]$ and $[L_{i\min}\ U_{i\max}]$ of the variable $x_j^{(fp)}$ ($j = 1$ to 6, i.e., ε'_{rp1} to ε'_{rp3} and ε''_{ip1} to ε''_{ip3}) is defined as the min (max) value of FDS in Fig. 5(a) and (b).

Step 3:

The variable $x_j^{(fp)}$ ($j = 7$ and 8, i.e., ξ' and ξ'') are initialized within the intervals $[0.1, 3]$ and $[0.2, 5]$ according to the literature [18].

Step 4:

The average values of all satisfied solutions of $x_j^{(fp)}$ in frequency point fp are calculated by using the following equation:

$$\bar{x}_j^{(fp)} = \sum_{s=1}^{TN} x_{js}^{(fp)} / TN, s.t. \begin{cases} j = 1, 2, \ldots, 8 \\ f_p = 1, 2, \ldots, 25 \end{cases} \quad (26)$$

which is used to constraint the value space of the next point, i.e., $fp+1$, where TN is the total number of solutions.

Step 5:

The frequency dependence is used to develop the constraint of amplitude range and change rate. The following equations are used to define the upper and lower bounds of the solutions in the next frequency point when $fp \leq 8$:

$$\text{upper bound} \begin{cases} x_j^{(fp+1)} < U_{r\max}, j = 1, 2, 3 \\ x_j^{(fp+1)} < U_{i\max}, j = 4, 5, 6 \end{cases} \quad (27)$$

$$\text{lower bound} \begin{cases} x_j^{(fp+1)} > [lb_{r1}, lb_{r2}, lb_{r3}]^T \cdot \bar{x}_j^{(fp)}, \\ j = 1, 2, 3 \\ x_j^{(fp+1)} > [lb_{i1}, lb_{i2}, lb_{i3}]^T \cdot \bar{x}_j^{(fp)}, \\ j = 4, 5, 6 \end{cases} \quad (28)$$

where lb_r and lb_i are the lower bound (amplitude) coefficients, which are less than 1.

It is worth noting that amplitude coefficients are used to determine the value range of the next frequency point based on the value of the present point. Using an imaginary part value as an example, Fig. 10 demonstrates how to use the amplitude coefficients and present point (fp) to determine the value range of the next sample point ($fp+1$). Additionally, amplitude

coefficients vary with changing frequency, which may be estimated using experimental records and data analysis of observed FDS data for oil-immersed insulation with varying degrees of aging.

Step 6:

If $8 < fp \leq 16$ (i.e., in medium-frequency intervals), the following equation is used to update the definition of the upper bound:

$$\text{upper bound} \begin{cases} x_j^{(fp+1)} < [ub_{r1}, ub_{r2}, ub_{r3}]^T \cdot \bar{x}_j^{(fp)}, \\ j = 1, 2, 3 \\ x_j^{(fp+1)} < [ub_{i1}, ub_{i2}, ub_{i3}]^T \cdot \bar{x}_j^{(fp)}, \\ j = 4, 5, 6 \end{cases} \quad (29)$$

where ub_r and ub_i are the upper limit coefficients, and the lower limit coefficient is also (28), i.e., $ub_i \geq 1 \geq ub_r > lb_r > lb_i > 0$.

Step 7:

If $16 < fp \leq 25$ (i.e., in high-frequency intervals), Fig. 5 shows that the real part of the FDS curve slowly decays and finally flatten in this interval, and the following equation is thus used to define the upper (lower) bound of variable $x_j^{(fp)}$ ($j = 1$ to 3)

$$L_{r\min} \leq x_j^{(fp+1)} < \bar{x}_j^{(fp)}, j = 1, 2, 3. \quad (30)$$

On the contrary, in Fig. 5, the imaginary part of the FDS curve decays until it reaches the "valley," and then gradually rises the curve. Thus, the gradient calculation

$$\text{grad}(x_j^{(fp)}) = \frac{\partial x_j(\omega + \Delta\omega)}{\partial(\omega + \Delta\omega)}, s.t. \begin{cases} j = 4, 5, 6 \\ grad > 0, \text{rise} \\ grad \leq 0, \text{decay} \end{cases} \quad (31)$$

is used to define the upper (lower) bound during two different states, as shown in the following equations:

$$\text{if rise, } \bar{x}_j^{(fp)} < \bar{x}_j^{(fp+1)} < [ub_{r1}, ub_{r2}, ub_{r3}]^T \cdot \bar{x}_j^{(fp)} \quad (32)$$

$$\text{if decay, } L_{i\min} \leq \bar{x}_j^{(fp+1)} < [ub_{r1}, ub_{r2}, ub_{r3}]^T \cdot \bar{x}_j^{(fp)}. \quad (33)$$

Step 8:

The value range of the next point ($fp+1$) can be determined by the amplitude factor and the current point (fp). Thus, when calculating the next point, all solutions in the above value range are considered to be valid, and the average value of these solutions is considered to be the final output. Then, perform $fp = fp+1$ until it reaches the maximum value to form the solutions corresponding to 25 frequency points, otherwise, return to Step 4.

Step 9:

Finally, the obtained $x_j^{(fp)}$ ($j = 1$ to 6) represent the complex relative permittivity of three single oil-immersed pressboards contained in the same composite structure (shown in Fig. 3), also, $x_j^{(fp)}$ ($j = 3$ and 6, i.e., ε'_{rp3} and ε''_{rp3}) is exactly the FDS data of the hotspot region in the entire system.

TABLE III
INITIAL VALUES OF UTILIZED PARAMETERS IN THE PROPOSED MODEL

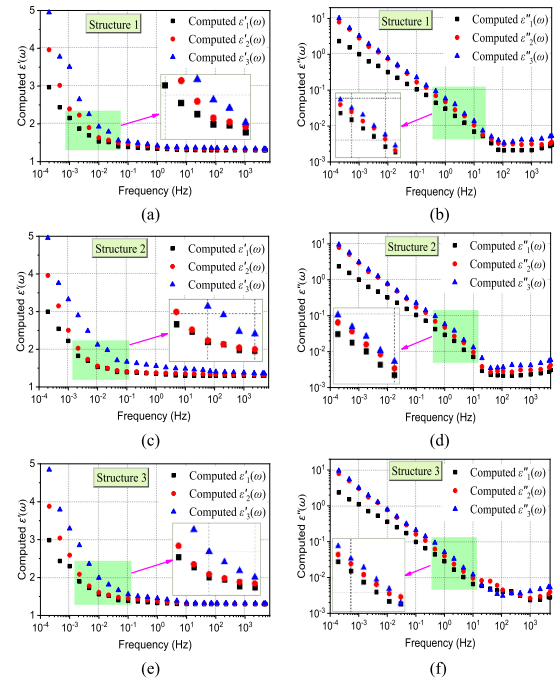| Label	Definition	Values and remarks
1. Parameters used in multi-objective function		
$\varepsilon^{*}_{\text{rtot}}$	The ε^{*} of insulation system	Shown in Fig. 5 (c) and (d)
$\varepsilon^{*}_{\text{ro}}$	The ε^{*} of oil	Shown in Fig. 5 (e) and (f)
X, Y	Geometric parameter of composite structure	X=0.33, Y=0.25 (by using (2))
m	Number of aging states	m=3 (three aging states in a structure)
2. Parameters used in NSGA		
PS	Population size	PS =200 (default value)
Gen	Generations	Gen = PS×number of variables
CP	Crossover probability	CP= 0.8 (default value)
MI	Migration interval	MI=20 (default value)
MP	Mutation probability	MP=0.001 (default value)
g_s	Linear inequality constraints	$\begin{cases} 0 < x_j^{(fp)}, j=1,2,...6 \\ 0.1 < x_7^{(fp)} < 3 \\ 0.2 < x_8^{(fp)} < 5 \end{cases}$ $\begin{cases}\sum_{j=1}^{3} x_j^{(fp)} > 3L_{\text{rmin}} \\ \sum_{j=4}^{6} x_j^{(fp)} > 3L_{\text{imin}}\end{cases}$ $\begin{cases} x_j^{(fp)} - x_{j+1}^{(fp)} < 0, j = 1,2 \text{ or } 4,5 \\ x_{j+2}^{(fp)} - x_{j+1}^{(fp)} - x_j^{(fp)} < 0, j = 1 \text{ or } 4 \end{cases}$
α_{pf}	Penalty factor	$\alpha_{pf} = \text{CP} + L_{\text{rmin}}^{\text{Gen}/L_{\text{rmin}}}$
3. Parameters used in the multi-constraint of NSGA		
TN	Total number of Pareto optimal solution	TN∈[13, 70] (According to the data record during the calculation)
lb_r, lb_i	Amplitude coefficient of the lower bound	$\begin{bmatrix} lb_{r1} & lb_{r2} & lb_{r3} \\ lb_{i1} & lb_{i2} & lb_{i3} \end{bmatrix} = \begin{bmatrix} 0.80, 0.75, 0.70 \\ 0.60, 0.55, 0.50 \end{bmatrix}$
ub_r, ub_i	Amplitude coefficient of the upper bound	$\begin{bmatrix} ub_{r1} & ub_{r2} & ub_{r3} \\ ub_{i1} & ub_{i2} & ub_{i3} \end{bmatrix} = \begin{bmatrix} 1.00, 0.97, 0.95 \\ 1.20, 1.20, 1.20 \end{bmatrix}$
L_{rmin}, U_{rmin}	Min/max value of ε'_{rp}	[1.3, 8] (Min/max values in Fig. 5a)
L_{imin}, U_{imin}	Min/max value of $\varepsilon''_{\text{rp}}$	[0.01, 12] (Min/max values in Fig. 5b)

Fig. 11. Computer FDS of (three) single oil-immersed pressboards in the same composite structure. (a) and (b) Real and imaginary parts of pressboards in structure 1. (c) and (d) Real and imaginary parts of pressboards in structure 2. (e) and (f) Real and imaginary parts of pressboards in structure 3.

V. FEASIBILITY INVESTIGATION ON FDS EXTRACTION OF OIL-IMMERSED INSULATION AT HOTSPOT REGION

A. Investigation Scheme and Parameters Assignment

In Section IV, the dielectric response equivalent circuit is applied to construct the multiobjective functions. The NSGA is later used to solve these functions to form a Pareto front that satisfies the multiobjective functions. Finally, a multiconstraint scheme of NSGA (MC-NSGA) is introduced to confirm the unique solution of the FDS data of the hotspot point by point.

Out of Table II, the total FDS data of structures 1–3 is measured as the data source to access the FDS data of the hotspot. Moreover, since the single pressboard 4 (PB4) contained in each structure conveys the worst aging states, thus, the FDS of pressboard 4 is regarded as the measured data of hotspot and later used for verification. The smaller the disagreement between the measured value and the calculated value of hotspot, the higher the extraction accuracy of the proposed model. To achieve the procedure described in Fig. 6 to acquire the FDS of the hotspot region, Table III presented the initial values of variables and parameters used in the proposed MC-NSGA model.

B. Accessing the FDS Data of Single Pressboard From Total FDS of Composite Structure

Substituting the total FDS data of composite structures 1–3, i.e., $\varepsilon^{*}_{\text{rtot}}$, into the defined procedure shown in Fig. 6, the unique solution of $x_j^{(fp)}$ (i.e., $\varepsilon^{*}_{\text{rp}i}$) can be computed point by point until it forms a continuous curve, then the resulting FDS data of three single oil-immersed pressboards contained in the same composite structure (i.e., $\varepsilon'_{\text{rp1}}$ to $\varepsilon'_{\text{rp3}}$ and $\varepsilon''_{\text{rp1}}$ to $\varepsilon''_{\text{rp3}}$) is plotted in Fig. 11. Especially, according to the assumption in

Section II, the data of $\varepsilon^{*}_{\text{rp3}}$ are regarded as the data of the hotspot in each composite structure.

From Fig. 11, the low-frequency FDS of insulation at the hotspot region ($\varepsilon^{*}_{\text{rp3}}$) is higher than the data at other positions. Such a result can be also observed in the literature [12]. The aging effect shortens the cellulose fiber's length and degrades its amorphous area and hydrogen bond, resulting in a decrease in internal intermolecular stress. In this circumstance, more age by-products and oil can stick to the cellulose fiber, increasing the number of oil-paper and other microinterfaces and enhancing the strength of the interfacial polarization. Additionally, as the temperature rises, the insulation ages more rapidly, and the concentration of aging by-products increases [8]. Since the typical (weak) polar aging by-products will contribute to the strength of the low-frequency interface polarization, in this case, the low-frequency FDS data of insulation at the hotspot region are thus higher than FDS data collected at other positions.

C. Contrastive Analysis of Extracted FDS of Hotspot

The feasibility verification of the proposed model is implemented by comparing the computed FDS data of the hotspot region with the measured data (twice measurements and marked as #1 and #2), which is shown in Fig. 12. The accuracy of the results depends on the generated disagreement between the computed values ($\varepsilon^{*}_{\text{c}}$) and the average values of measurement data ($\varepsilon^{*}_{\text{m}}$). The following equation is used to quantify the
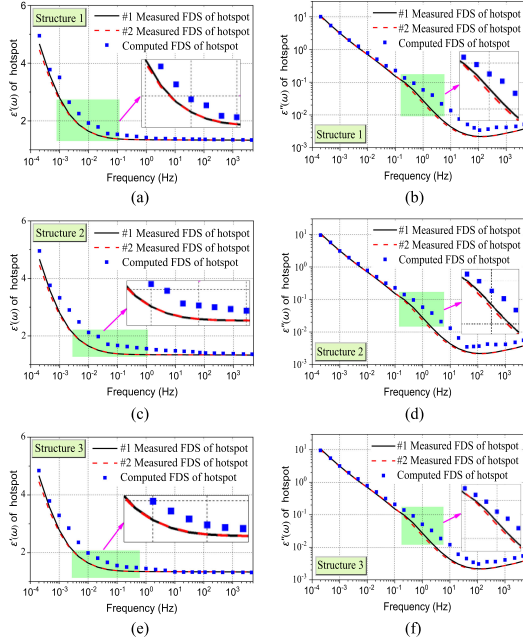
Fig. 12. Comparison of the computed FDS data of hotspot with the measured data. (a) and (b) Real and imaginary data of hotspot in structure 1. (c) and (d) Real and the imaginary data of hotspot in structure 2. (e) and (f) Real and the imaginary data of hotspot in structure 3.

TABLE IV
STATISTICS OF CALCULATION RESULTS

Structure	Structure 1	Structure 2	Structure 3	Average
Real part	0.235	0.304	0.242	0.260
Imaginary part	0.078	0.195	0.177	0.150

standard deviation (STD) of the obtained results:

$$STD = \sqrt{\frac{1}{25} \times \sum\nolimits_{\omega=1}^{25} \left[\bar{\varepsilon}_m^*(\omega) - \varepsilon^*{}_c(\omega)\right]^2}. \quad (34)$$

The statistics results are listed in Table IV. Thus, the statistics result preliminarily proves the accuracy of the reported model.

As mentioned in Section II, the *XY* model [16] can calculate the average FDS data of solid insulation by using the FDS data of the entire insulation system and insulating oil. Thus, taking the composite structure 1 [shown in Fig. 5(c) and (d)] as an example, we compared the FDS of solid insulation at hotspot [represented in Fig. 12(a) and (b)] to the composite structure 1's average FDS (calculated using the *XY* model) and total FDS, as shown in Fig. 13.

The FDS data for the composite insulation structure are significantly higher than the other two values since it includes the contribution of insulating oil and insulation geometry. Thus, in any site trials, the FDS data for the entire insulation system cannot be directly used to determine the state of aging of its solid insulation.

Additionally, the hotspot's FDS data are much greater than the average FDS. The average relative error (RE) of the real (imaginary) component ranges between 38.03% and 107.35%,
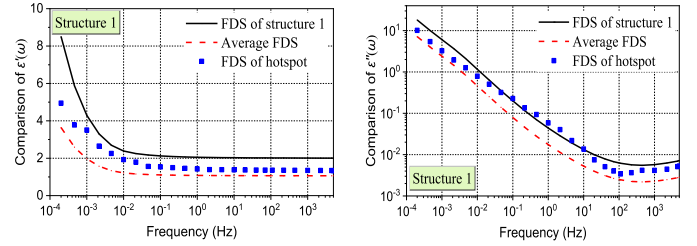

Fig. 13. Comparison among the FDS of composite structure, average FDS of solid insulation, and FDS of insulation at the hotspot.

as determined by the following equation:

$$RE(\%) = \frac{|\text{Hotspot data} - \text{Average data}|}{\text{Average data}} \times 100\%. \quad (35)$$

Thus, using average data during state evaluation would result in a significant underestimation of the insulating system's degeneration.

VI. CONCLUSION

Current research reveals that the "inverse process" can be regarded as a multiobjective optimization problem to obtain the hotspot's FDS data. The modified *XY* model may be used to construct multiobjective functions; the frequency dependence of dielectric materials is beneficial to develop the MC-NSGA model, then, final results of FDS data of hotspot region can be achieved. According to the verification experiment, the average STD is less than 0.26. The findings indicate that using average FDS data for the status evaluation would result in a significant underestimation of the insulation system's deterioration.

At present, the application of this model to lab trials is under consideration in different conditions. Regarding the received feedback, critical improvements must be made in due course. These include generalizing the model to include more aging states, modifying the model to account for nonuniform aging along the axial direction, and quantifying the model's aging states using feature parameters from the distributed relaxation model. Also, it is hoped to have some results to site trials in further research.

REFERENCES

[1] J. I. Aizpurua, S. D. J. McArthur, B. G. Stewart, B. Lambert, J. G. Cross, and V. M. Catterson, "Adaptive power transformer lifetime predictions through machine learning and uncertainty modeling in nuclear power plants," *IEEE Trans. Ind. Electron.*, vol. 66, no. 6, pp. 4726–4737, Jun. 2019.

[2] Y. Wu, P. J. Zhang, and G. H. Lu, "Detection and location of aged cable segment in underground power distribution system using deep learning approach," *IEEE Trans. Ind. Electron.*, vol. 17, no. 11, pp. 7379–7389, Nov. 2021.

[3] W. Liao, L. Zhou, D. Wang, A. Wang, L. Guo, and Y. Cui, "A diagnostic method for moisture intrusion fault in OIP bushing," *IEEE Trans. Instrum. Meas.*, vol. 69, no. 9, pp. 7072–7081, Sep. 2020.

[4] L. S. Liu, H. Mei, C. Guo, Y. Tu, and L. Wang, "Pixel-level classification of pollution severity on insulators using photothermal radiometry and multiclass Semisuper-vised support vector machine," *IEEE Trans. Ind. Electron.*, vol. 17, no. 1, pp. 441–449, Jan. 2021.

[5] J. F. Liu *et al.*, "Moisture diagnosis of transformer oil-immersed insulation with intelligent technique and frequency-domain spectroscopy," *IEEE Trans. Ind. Informat.*, vol. 17, no. 7, pp. 4624–4634, Jul. 2021.

[6] S. Kumar, L. Kumar, T. Islam, and K. K. Raina, "Condition monitoring of transformer breather using a capacitive moisture sensor," *IEEE Trans. Ind. Electron.*, vol. 67, no. 11, pp. 9779–9789, Nov. 2020.

[7] A. Baral and S. Chakravorti, "Assessment of non-uniform aging of solid dielectric using system poles of a modified debye model for oil-paper insulation of transformers," *IEEE Trans. Dielectr. Elect. Insul.*, vol. 20, no. 5, pp. 1922–1933, Oct. 2013.

[8] W. D. Sun *et al.*, "Improved method for aging assessment of winding Hot-spot insulation of transformer based on the 2-FAL concentration in oil," *Int. J. Elect. Power*, vol. 112, pp. 191–198, Nov. 2019.

[9] V. Vasovic *et al.*, "Aging of transformer insulation of experimental transformers and laboratory models with different moisture contents: Part II – Moisture distribution and aging kinetics," *IEEE Trans. Dielectr. Elect. Insul.*, vol. 26, no. 6, pp. 1847–1852, Dec. 2019.

[10] H. Karami, H. Tabarsa, G. B. Gharehpetian, Y. Norouzi, and M. A. Hejazi, "Feasibility study on simultaneous detection of partial discharge and axial displacement of HV transformer winding using electromagnetic waves," *IEEE Trans. Ind. Electron.*, vol. 16, no. 1, pp. 67–76, Jan. 2020.

[11] G. Lu and P. J. Zhang, "A novel leakage-current-based online insulation monitoring strategy for converter transformers using common-mode and differential-mode harmonics in VSC system," *IEEE Trans. Ind. Electron.*, vol. 68, no. 2, pp. 1636–1645, Feb. 2021.

[12] L. Zhou, D. Wang, L. Guo, L. Wang, J. Jiang, and W. Liao, "FDS analysis for multilayer insulation paper with different aging status in traction transformer of high-speed railway," *IEEE Trans. Dielectr. Elect. Insul.*, vol. 24, no. 5, pp. 3236–3244, Oct. 2017.

[13] A. K. Jonscher, "Dielectric relaxation in solids," *J. Phys. D, Appl. Phys.*, vol. 32, no. 14, pp. 57–70, 1999.

[14] A. Baral and S. Chakravorti, "A modified Maxwell model for characterization of relaxation processes within insulation system having non-uniform aging due to temperature gradient," *IEEE Trans. Dielectr. Elect. Insul.*, vol. 20, no. 2, pp. 524–534, Apr. 2013.

[15] Y. Cui, H. Ma, T. Saha, and Y. L. Liu, "Understanding the effect of non-uniform ageing on dielectric response of transformer insulation," in *Proc. IEEE Power Energy Soc. Gen. Meeting*, 2017, pp. 1–5.

[16] T. K. Saha and P. Purkait, "Investigations of temperature effects on the dielectric response measurements of transformer oil-paper insulation system," *IEEE Trans. Power Del.*, vol. 23, no. 1, pp. 252–260, Jan. 2008.

[17] J. F. Liu *et al.*, "A modified X-model of the oil-impregnated bushing including non-uniform thermal aging of cellulose insulation," *Cellulose*, vol. 27, pp. 4525–4538, Mar. 2020.

[18] X. H. Fan *et al.*, "A modified XY model of transformer oil-paper insulation system including non-uniform aging and conductance effect," *IET Gener. Transmiss., Distrib.*, vol. 15, no. 13, pp. 2008–2017, Mar. 2021.

[19] D. Y. Wang *et al.*, "A new testing method for the dielectric response of oil-immersed transformer," *IEEE Trans. Ind. Electron.*, vol. 67, no. 12, pp. 10833–10843, Dec. 2020.

[20] M. S. Mohammed and R. A. Vural, "NSGA-II+FEM based loss optimization of three-phase transformer," *IEEE Trans. Ind. Electron.*, vol. 66, no. 9, pp. 7417–7425, Sep. 2019.

[21] A. Abu-Siada, M. I. Mosaad, D. Kim, and M. F. El-Naggar, "Estimating power transformer high frequency model parameters using frequency response analysis," *IEEE Trans. Power Del.*, vol. 35, no. 3, pp. 1267–1277, Jun. 2020.

[22] D. Ahmed and L. Wang, "Noniterative design of Litz-wire high-frequency gapped-transformer (Lw-HFGT) for LLC converters based on optimal core-geometry factor model (OKGM)," *IEEE Trans. Ind. Electron.*, vol. 68, no. 4, pp. 3090–3102, Apr. 2021.
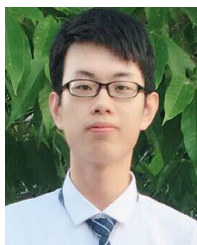
Jiefeng Liu (Member, IEEE) received the M.S. and Ph.D. degrees in electrical engineering from Chongqing University, Chongqing, China, in 2011 and 2015, respectively.

In 2018, he joined Guangxi University, Nanning, China, where he is an Associate Professor. His research interests include the field of condition assessment and fault diagnosis for oil–paper insulation.

Hui Hwang Goh (Senior Member, IEEE) received the B.Eng.(Hons.) and M.Eng. degrees in electrical Engineering, and the Ph.D. degree in electrical engineering from the Universiti Teknologi Malaysia, Johor, Malaysia, in 1998, 2002, and 2007, respectively.

He is currently a Professor of Electrical Engineering with Guangxi University, Nanning, China. His research interests include embedded power generation modeling and simulation, power quality studies, multicriteria decision-making, and dynamic equivalent.

Dr. Goh is a Fellow of the Institution of Engineering and Technology, U.K., and the Chinese Society of Electrical Engineering, and a Chartered Engineer under the Engineering Council United Kingdom.

Yiyi Zhang (Member, IEEE) received the B.Eng. degree from Guangxi University, Nanning, China, in 2008, and the Ph.D. degree from Chongqing University, Chongqing, China, in 2014, both in electrical engineering.

In 2014, he joined Guangxi University, where he is currently an Associate Professor. His current research interests include the intelligent diagnosis for transformers.

Chaohai Zhang (Member, IEEE) received the B.A. degree from the Harbin Institute of Technology, Harbin, China, in 1985, the M.S. degree from the Navy Aeronautical Engineering Academy, Yantai, China, in 1988, and the Ph.D. degree from Hong Kong Polytechnic University, Hong Kong, in 2002, all in electrical engineering.

He is currently a JSPS Research Fellow with Kumamoto University, Japan, a Research Engineer in Canada, and the Chief Research Scientist with State Grid EPRI in China. His current research focuses on high-voltage engineering.

Saifur Rahman (Life Fellow, IEEE) received the B.Sc. degree from the Bangladesh University of Engineering and Technology, Dhaka, Bangladesh, in 1973, and the Ph.D. degree from Virginia Polytechnic Institute and State University, Blacksburg, VA, USA, in 1978, both in electrical engineering.

He was the President-elect of the IEEE in 2022. He is currently the Director for the Advanced Research Institute, Virginia Polytechnic Institute and State University, Blacksburg, VA, USA, where he is also the Joseph Loring Professor of Electrical and Computer Engineering and also directs the Center for Energy and the Global Environment. He is currently a Guest Professor with Guangxi University, Guangxi, China. He has authored or coauthored in the areas of his research interests which include smart grids, conventional and renewable energy systems, load forecasting, uncertainty evaluation, infrastructure planning, and IoT device integration.

Dr. Rahman was the President of IEEE Power and Energy Society for 2018 and 2019. He was the Vice-President of the IEEE Publications Board and as a member for the IEEE Board of Directors in 2006. He was the Founding Editor-in-Chief for the IEEE TRANSACTIONS ON SUSTAINABLE ENERGY and IEEE ELECTRIFICATION MAGAZINE.

Xianhao Fan received the B.Eng. degree in electrical engineering in 2018 from Guangxi University, Guangxi, China, where he is currently working toward the Ph.D. degree in electrical engineering.

His current research interests include intelligent optimization, machine learning, and dielectric response techniques.